Colloidal phase behavior of high aspect ratio clay nanotubes in symmetric and asymmetric electrolytes

Claire Hotton, Léna Le Roux, Claire Goldmann, Stéphan Rouzière, Pascale Launois, Thomas Bizien, Erwan Paineau

Graphical abstract:

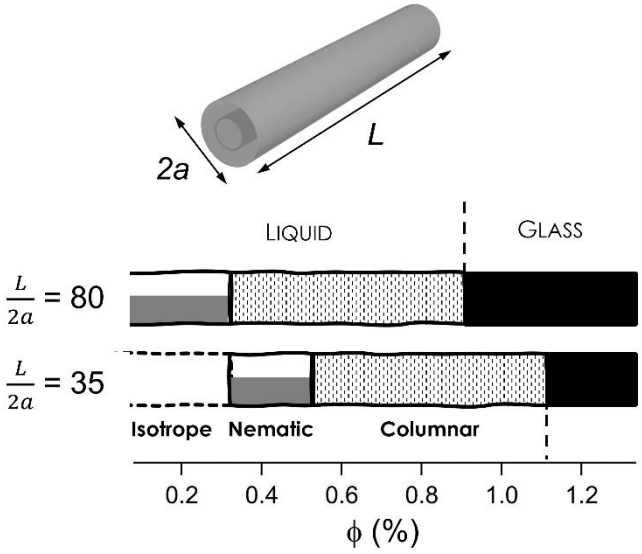

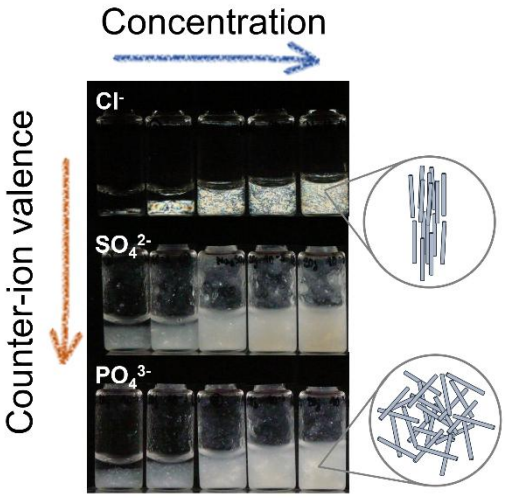

Colloidal phase behavior of high aspect ratio clay nanotubes in symmetric and asymmetric electrolytes

Claire HOTTON[a,*], Léna LE ROUX[a], Claire GOLDMANN[a], Stéphan ROUZIÈRE[a], Pascale LAUNOIS[a], Thomas BIZIEN[b], Erwan PAINEAU[a,*]

[a] Université Paris-Saclay, CNRS, Laboratoire de Physique des Solides, Orsay, 91405, France

[b] Synchrotron SOLEIL, L'Orme des Merisiers, 91192 Gif-sur-Yvette Cedex, France

* Corresponding authors:

Laboratoire de Physique des Solides, Université Paris-Saclay, Bat.510, 1 rue Nicolas Appert, 91405 Orsay, France.

claire.hotton@universite-paris-saclay.fr. Phone: +33 (0) 1 69 15 53 94

erwan-nicolas.paineau@universite-paris-saclay.fr. Phone: +33 (0) 1 69 15 60 51

Abstract

Hypothesis: Imogolite nanotubes (INTs) are unique anisometric particles with monodisperse nanometric diameters. Aluminogermanate double-walled INTs (Ge-DWINTs) are obtained with variable aspect ratios by controlling the synthesis conditions. It thus appears as an interesting model system to investigate how aspect ratio and ionic valence influence the colloidal behavior of highly anisometric rods.

Experiments: The nanotubes were synthesized by hydrothermal treatment for 5 or 20 days to modify the aspect ratio while the electrostatic interactions were investigated by comparing the colloidal stability in symmetric and asymmetric electrolytes. The phase behavior and their related microstructure were determined by optical observations and small-angle X-ray scattering measurements, coupled with interparticle distance modelling.

Findings: We revealed that colloidal suspensions of Ge-DWINTs prepared in NaCl are guided by repulsive double layer forces, undergoing different liquid crystal phase transitions before stiffen into a glass-like state. We found that the microstructure can be rationalized by taking into account the anisometric nature of the particles. By contrast, dispersions prepared with asymmetric electrolytes are governed by strong attractive forces and thus form space-filling gels containing large nanotubes aggregates.

Keywords: imogolite, self-organization, SAXS, columnar phase, glass, gel, phase diagram

1. Introduction

Inorganic nanoparticles, whether natural or synthesized, present a wide variety of forms (rods, cylinders, disks, polyhedrons…), making them appealing for applications [1,2]. Most of the shapes are intrinsically anisometric as the aspect ratio between the lengths of the major axis and the minor axis is always larger than 1. The aspect ratio is a fundamental parameter governing the self-organization of anisometric nanoparticles dispersed in a solvent. According to statistical mechanics theories and computer simulations [3–5], anisometric nanoparticles may undergo entropy-driven phase transitions due to excluded-volume interactions. The excluded volume is the effective volume occupied by the particle under the effect of Brownian motion. In the dilute regime, when the nanoparticles are not interacting with each other, it corresponds to a sphere whose diameter is defined by the largest dimension of the objects. In this case, the nanoparticles explore all orientational configurations and the phase is described as isotropic. When the concentration of nanoparticles increases, a competition between orientational entropy (favoring the isotropic phase) and packing entropy (favoring long-range ordered phases) occurs. Another important effect is the presence of surface charges on the nanoparticles that impact their colloidal stability due to a subtle balance of electrostatic interactions. The balance is dependent of the nature (symmetric or asymmetric salts, ion valence) and concentration of the electrolytes, also referred as the ionic strength (I). One way of studying these systems is to explore their phase diagrams as a function of the nanoparticle aspect ratio and volume fraction.

A wide variety of anisometric charged nanoparticles display spontaneous phase transitions from a disordered (isotropic) to long-range ordered states (nematic, smectic, lamellar, columnar...) as well as microstructures with arrested dynamics such as gels and glasses with increasing particle concentration [6–11]. A typical example is the colloidal behavior of swelling clay minerals that

has been thoroughly explored for almost 100 years due to their large aspect ratio. Observations of lyotropic liquid-crystalline phases have remained elusive until recently with the occurrence of an isotropic-to-nematic phase transition in aqueous dispersions of swelling clay nanosheets (nontronite [12,13], beidellite [14] or fluorohectorite [15,16]). The aspect ratio of 2D clay objects has been proven to influence the resulting colloidal behavior by modifying the position of both the isotropic-to-nematic transition and the sol/glass transition [17,18]. By contrast, the fate of self-organization with one-dimensional (1D) clay nanoparticles such as halloysite or sepiolite received less attention, probably because most of these nanoparticles do not spontaneously present ordered phases unless stabilized by functionalization [19,20]. Beyond 1D clay nanoparticles, phase stabilization is a recurring phenomenon when studying the colloidal stability of objects such as nanotubes. For example, different methods have been explored for dispersing carbon and boron nitride nanotubes [21–26], including covalent functionalization, stabilization with DNA or surface protonation, allowing favorable conditions for the occurrence of nematic liquid crystals. Furthermore, carbon nanotubes present polydisperse diameters and lengths after synthesis, requiring size-sorting procedure. Their aspect ratio has been proved to play a significant role on the electrical, mechanical or thermal properties of carbon nanotubes-based composites [27–29], but not specifically on their colloidal behavior.

In this context, imogolite clay nanotubes $(OH)_3Al_2O_3(Si,Ge)(OH)$ appear as a perfect model system due to their monodisperse nanometric diameters and the possibility to form stable dispersions in water without functionalization or the use of strong acid [30]. These nanotubes display spontaneously nematic [31–33] and/or hexagonal columnar phases [34,35] when the concentration in particles is increased. The colloidal stability of imogolite nanotubes (INTs) is related to their surface charge, which is mainly due to the protonation of external aluminol groups ($\equiv Al_2OH$ and $\equiv$Al-OH) [36–38]. Typically, the electrophoretic mobility of imogolite nanotubes

is always positive (> 40 mV at pH = 7) with a point of zero charge beyond pH = 10 [34,38]. The self-organization of imogolite nanotubes can be controlled by adjusting the range of double layer electrostatic repulsions through the ionic strength (e.g. $I < 10^{-2}$ mol.L^{-1} for symmetric monovalent salt) [30,39]. An advantage of imogolite nanotubes is the ability to modify their structure by changing either the nature (chloride, perchlorate, nitrate, alkoxide…) or the ratio of the precursors during their hydrothermal synthesis. A slight variation of these parameters can induce structural vacancies in the nanotube walls or modify the morphology, thus dramatically affecting the self-organization behavior [40,41].

Studies investigating the specific ion effects (apart from NaCl) on the colloidal stability of 1D objects are limited, to the best of our knowledge, to cellulose nanorods, showing the influence of the nature of the salts on the aggregation kinetics [42] or the modulation of the chiral nematic structure [43]. There is still a gap to be filled to determine how ion specificity effects can modulate the colloidal behavior of stiff nanotubes. Understanding the specific effects of electrolytes is currently of significant interest for bottom-up assembly of anisometric nanotubes into functional metamaterials such as fibers or films [24,26,44]. Most studies on INTs colloidal stability use monovalent salts, generally NaCl. Kobayashi *et al.* recently investigated the influence of ionic valence *z* and ion specificity (degree of hydration, ligand exchange capacity…) on the stabilization and aggregation of allophane [45–47], a hollow spherical clay nanoparticle with a structural formula close to imogolite. They demonstrated the validity of Derjaguin-Landau and Verwey-Overbeek (DLVO) theory for the accurate prediction of the colloidal stability of these natural spherical nanoparticles with multivalent counter-anions. For asymmetric salts, the magnitude of ion adsorption increases with the ionic valence if the counter-ions are oppositely charged to the particle [48]. Nevertheless, these nanostructures show no liquid crystal phase transitions unlike INTs.

Drawing on these previous studies, we investigate how the phase diagram of anisometric imogolite nanotubes is affected by asymmetric salts with respect to symmetric electrolytes while varying the aspect ratio (length/diameter) of the nanotubes. We synthesized aluminogermanate double-walled imogolite analogues (Ge-DWINTs) by adjusting the hydrothermal aging time (5 or 20 days) [49]. Series of dispersions with controlled ionic strength (10^{-3} mol.L^{-1}) were prepared with NaCl, Na_2SO_4 or Na_3PO_4 electrolytes. The value of the imposed strength was chosen based on previous studies showing that below 10^{-2} mol.L^{-1}, Ge-DWINTs dispersions are colloidally stable [30,39,41]. All the samples were characterized by coupling optical microscopy and small-angle X-ray scattering experiments. We explained the evolution of the microstructure on the basis of an effective geometrical approach taking into account the anisometric nature of the nanotubes. Finally, a complete phase diagram is established, where the effect of the ionic valence is discussed with respect to the nanotube concentration and aspect ratio.

2. Material and Methods

2.1. Synthesis of Ge-DWINTs with different aspect ratio

Aluminogermanate double-walled imogolite nanotubes were obtained following the procedure described by Amara *et al.* [50]. An aqueous solution of aluminum perchlorate nonahydrate (C = 0.2 mol.L^{-1}, reagent grade, Alfa Aesar), tetraethoxygermane (≥99.95%, Sigma-Aldrich) and urea (≥99%, Sigma-Aldrich) was prepared under stirring with a molar ratio of [Al]:[Ge]:[urea] equals to 2:1:2. The choice of hydrated perchlorate instead of anhydrous salt has been made to minimize any risk of exothermic reactions when mixing aluminum salt with water. The mixture was then transferred into a PTFE-lined acid digestion vessel (Parr Instrument) for hydrothermal aging during 5 or 20 days, referred to as DW_{5d} and DW_{20d} in the following. After hydrothermal treatment, the resulting suspensions were washed with ultrapure water using semipermeable

dialysis membranes (Spectra/Por®, cutoff = 10 kDa). The water bath was renewed at least 10 times thus allowing the conductivity to be dropped below 0.5 $mS.cm^{-1}$ [51]. Transmission electron microscopy (TEM) experiments were performed to determine the length distribution of the nanotubes. For both DW_{5d} and DW_{20d}, a dispersion was prepared at 1 $mg.L^{-1}$ in ethanol and a drop of it was deposited on a standard carbon-coated copper grid. TEM observations were carried out on a JEOL 1400 microscope operating at 80 kV. Image analysis was realized using Fiji software [52].

2.2. Colloidal dispersions with controlled ionic strength

Concentrated samples were prepared by osmotic stress by maintaining during two weeks semi-permeable membranes filled with DW_{5d} and DW_{20d} stocks in a 2L beaker containing a polyethylene glycol solution (M_w = 20000 $g.mol^{-1}$, C = 20 $g.L^{-1}$). An appropriate amount of NaCl, Na_2SO_4 or Na_3PO_4 salts was added to keep a constant ionic strength *I*, fixed at 10^{-3} M, according to:

$$I = \frac{1}{2}\sum_{i=1}^{n} c_i z_i^2 \quad (1)$$

with c_i the molar concentration of ions, z_i the charge number of ions and the index *i* runs over all the ions in the solution. After completion of the osmotic stress, the dispersions were recovered and their volume fractions ϕ ($\phi = C/\rho_{INT}$ with *C* the solid concentration of Ge-DWINTs and ρ_{INT} the density of a nanotube taken as 3.6 $g.cm^{-3}$ [44]) were determined by weight loss upon drying during 24h. For each batch, a series of samples has been prepared by dilution with the appropriate salt solution at $I = 10^{-3}$ M to obtain dispersions with varying volume fraction ranging from 0.07 to 2%. Macroscopic optical observations were performed using a home-made polarized-light observation setting equipped with a Panasonic DMC-FZ18 digital camera.

Polarized optical microscopy (POM) was carried out on a BX51-P (Olympus, Japan) either without or with the use of a retardation filter (l-plate at 530 nm) placed at 45° with respect to the polarizers. Images were acquired with a sCMOS color camera (sCMEX-20, Euromex, Netherlands). Aqueous dispersions were sucked into flat glass capillaries (0.2 x 2 mm, VitroCom, USA), which have been flame-sealed and stored vertically prior to POM observations.

2.3. Small-Angle X-ray scattering (SAXS)

Synchrotron-based SAXS experiments were realized at the SWING beamline (SOLEIL synchrotron, Saint-Aubin, France) and a fixed wavelength λ = 1.0332 Å. The scattering patterns were collected on a two-dimensional detector (Eiger 4M, Dectris Ltd., Switzerland) placed at a distance of 6.2 m of the sample in a vacuum tunnel. Prior to SAXS experiments, aqueous dispersions were transferred in cylindrical borosilicate glass capillaries (WJMGlas/Müller GmbH, DE) that were flame-sealed and stored vertically. Angular integration of the scattering patterns, giving the dependence of the scattered intensity as a function of the scattering vector modulus Q ($Q = 4\pi \sin(\theta) / \lambda$ with 2θ is the scattering angle) was processed by homemade software.

3. Results and discussion

3.1. Characterization of the nanotubes batches

We have demonstrated recently that long reaction times (> 5 days) further increase the length distribution and thus the aspect ratio [49]. The completion of Ge-DWINTs is attested by infrared spectroscopy and X-ray scattering (Figure S1), showing the classic signatures associated with these nanotubes (see Supporting Information). As shown previously, the synthesis conditions ensure the absence of polydispersity in the number of walls [50] and the outer radius a of double-walled aluminogermanate nanotubes is around 2.2 nm [40]. Transmission electron microscopy

observations and the related length distribution (Figure 1) confirm an increase in the proportion of tubes longer than 500 nm for DW_{20d}. In both 5 days and 20 days batches, nanotubes length follows a log-normal distribution with a mean value *L* around 150 nm for DW_{5d} and 350 nm for DW_{20d}. Moreover, the latter presents a significant proportion of nanotubes with length around 900 nm.

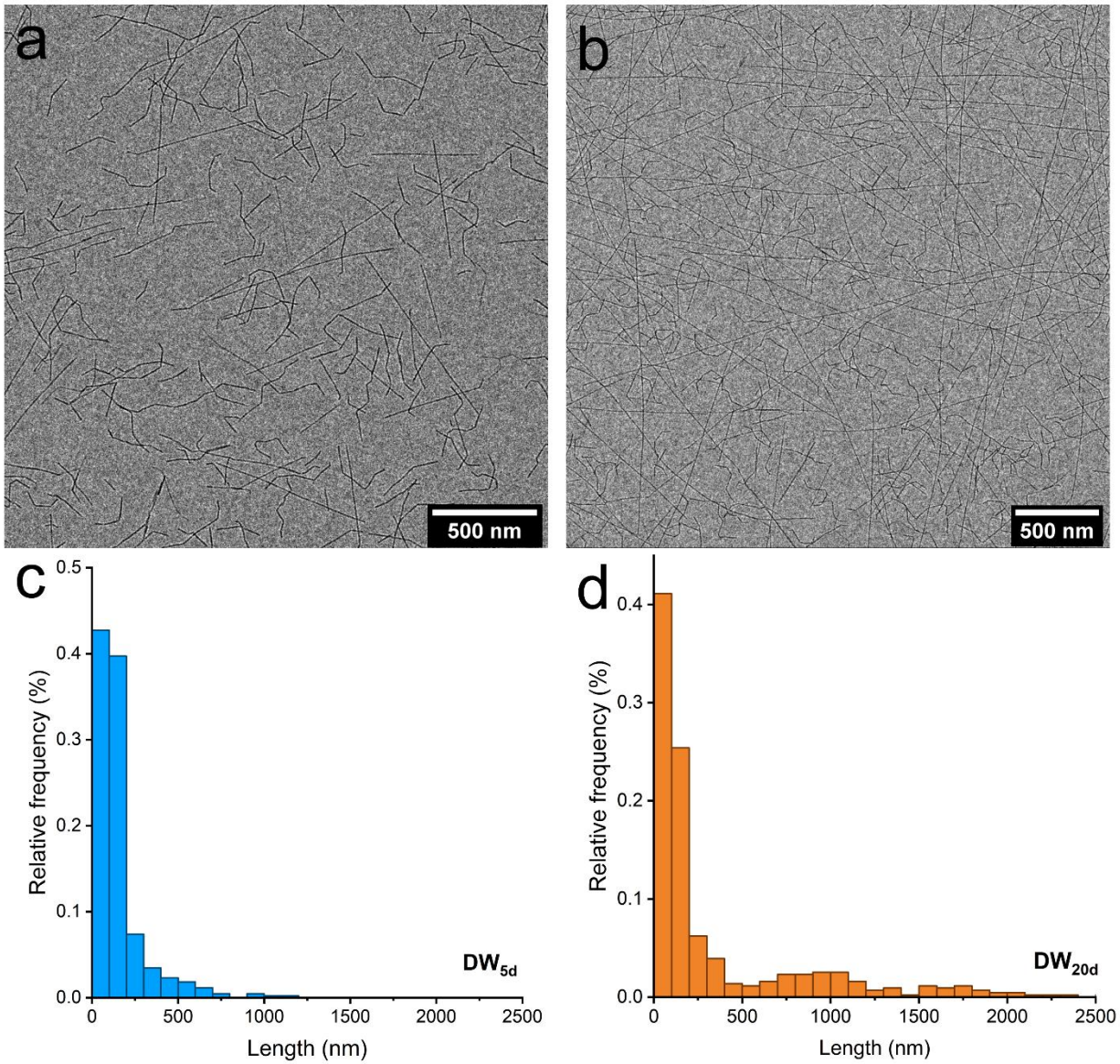

Figure 1. Representative TEM images of Ge-DWINTs batches obtained after (a) 5 days and (b) 20 days of hydrothermal reaction. Corresponding histograms of length distribution for (c) DW_{5d} and (d) DW_{20d}.

3.2. Phases transitions vs aggregation

Liquid-crystal (LC) phases can be revealed by studying the optical properties of the dispersions. Using NaCl to control the ionic strength allows the formation of stable Ge-DWINTs suspensions that are optically transparent under visible light [40]. By choosing thoroughly the initial precursors, typically perchlorate anions, these Ge-DWINTs dispersions can exhibit a rich liquid-crystalline phase behavior at low volume fraction (down to 0.2%) [40]. By contrast, dispersions of Ge-DWINTs prepared with Na_2SO_4 or Na_3PO_4 electrolytes are turbid under visible light suggesting the presence of larger structures rather than individual nanotubes. Investigations of the phase behavior of Ge-DWINTs dispersions at a fixed ionic strength ($I = 10^{-3}$ mol.L^{-1}) controlled by these different salts (NaCl, Na_2SO_4 and Na_3PO_4) are conducted as a function of the nanotube volume fraction and for each nanotube aspect ratio. Glass vials filled with these dispersions were left in an upright position during one month to ensure reaching thermodynamic equilibrium. Figure 2 presents the birefringence of Ge-DWINTs dispersions featured by naked-eye observations between crossed-polarizers.

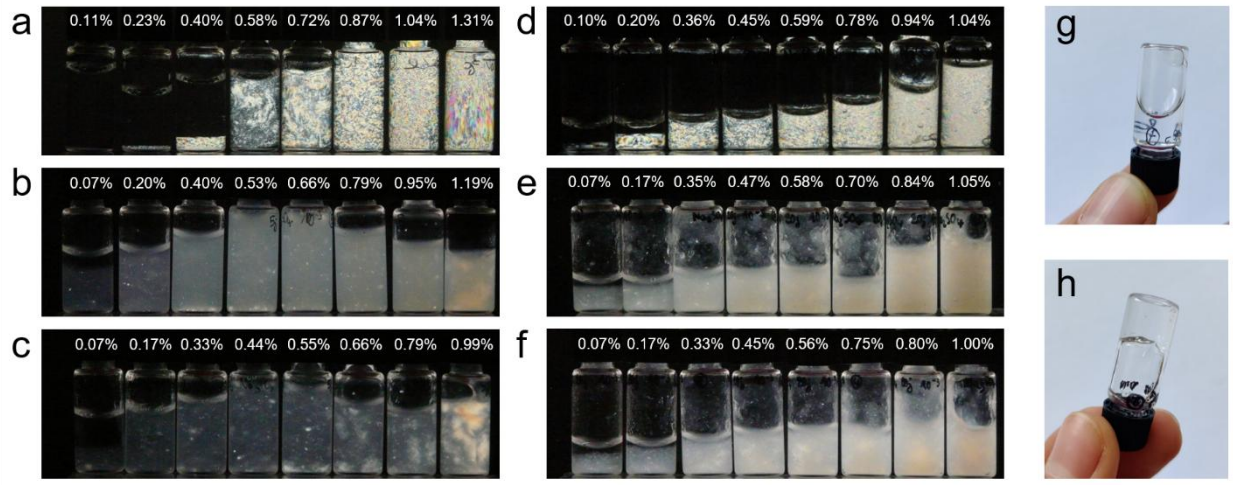

Figure 2. Macroscopic optical observations between crossed polarizers of (a-c) DW_{5d} and (d-f) DW_{20d} aqueous dispersions prepared at different volume fractions ϕ and electrolytes (IS = 10^{-3} $mol.L^{-1}$). (a,d) NaCl; (b,e) Na_2SO_4; (c,f) Na_3PO_4. Photographs of DW_{20d} aqueous dispersions with NaCl (g) in a liquid state (ϕ = 0.36%) and (h) above the glass transition (ϕ = 0.94%). The latter does not flow upon tube reversal.

In the case of NaCl electrolyte (Figure 2a,d), suspensions of Ge-DWINTs exhibit an isotropic phase at low volume fractions (less than 0.10%). A spontaneous phase separation occurs beyond a certain volume fraction (DW_{5d}: $\phi > 0.2\%$; DW_{20d}: $\phi \sim 0.1$ %) as shown by the coexistence of an isotropic phase with a denser birefringent LC phase. The isotropic phase at the top of the vial displays streaming birefringence when the samples are disturbed. This simple visual test tells us that the isotropic phase contains nanotubes, aligning within the flow upon shearing. The phase separation results from a thermodynamic equilibrium, the co-existence of the isotropic and LC phases reflecting a first order transition. The proportion of the birefringent phase raises with increasing the total volume fraction. By further increasing the volume fraction, liquid dispersions (Figure 2g) stiffen to form homogenous and transparent arrested phases (Figure 2h). These arrested phases remain birefringent between crossed polarizers, indicating that the nanotubes

have a preferred orientation. They can therefore be considered as a glass-like state, where the slowing of the nanotubes dynamics is due exclusively to excluded volume effects [6].

For dispersions prepared with divalent and trivalent salts (Figure 2b-f), the samples remain turbid with in some cases the presence of large and birefringent domains. A phase separation is observed only for the lowest volume fractions but the upper isotropic phase does not show any birefringence under flow. The phase separation is only due to the aggregation of nanotubes, which end up sedimenting in the vials. For $\phi > 0.2\%$, the samples display an arrested behavior, blocking the separation of large nanotubes clusters, independently of the nanotube aspect ratio. In this case, these samples can be considered as gels due to the attractive nature of the interactions.

3.3. Optical textures at the microscopic level

The nature of the different phases can be assessed through the study of the optical texture of the dispersions using polarized optical microscopy (POM). Representative POM images of DW_{5d} and DW_{20d} dispersions prepared in NaCl (Figure S2 and Figure 3) present various optical textures related to different LC phases as the volume fraction increases. In the case of DW_{20d} at ϕ = 0.10%, POM image displays a clear separation between an isotropic phase and a birefringent one. The texture is typical of the nematic phase [14,34], with smooth bright and dark regions related to the structural defects (disclinations lines) between the domains oriented in different directions as shown by observing the sample using a retardation filter while tilting the sample by ± 45° clockwise (Figure S3). In these images, blue (pink) regions correspond to an orientation of the nanotube long axis parallel (perpendicular) to the slow axis of the retardation filter. While increasing the concentration up to 0.45%, pleated ribbon like areas of aligned nanotubes are observed, highlighted by the modification of the optical paths when the λ-plate is inserted (Figure 3). This texture corresponds to the typical hexagonal columnar phase [40]. At higher

concentration (ϕ = 1.04%), DW_{20d} dispersions in NaCl form birefringent arrested phases that show flow alignment texture. The evolution of the optical textures for DW_{5d} dispersions in NaCl are similar although the phase transitions do not occur at the same volume fractions (Figure S2). The optical textures for samples with multivalent salts differ significantly since no LC phase can be identified (Figure 4). Ge-DWINTs dispersions prepared in Na_2SO_4 and Na_3PO_4 display almost similar POM images with the presence of birefringent aggregates whatever the concentration. However, the size and shape of the aggregates differ with the aspect ratio of the nanotubes as illustrated from POM images in Figure 4. Rounded aggregates are obtained with DW_{5d} samples as those observed previously for single-walled aluminogermanate nanotubes (aspect ratio around 11) [51], while the structures are more elongated for the highest nanotube aspect ratio.

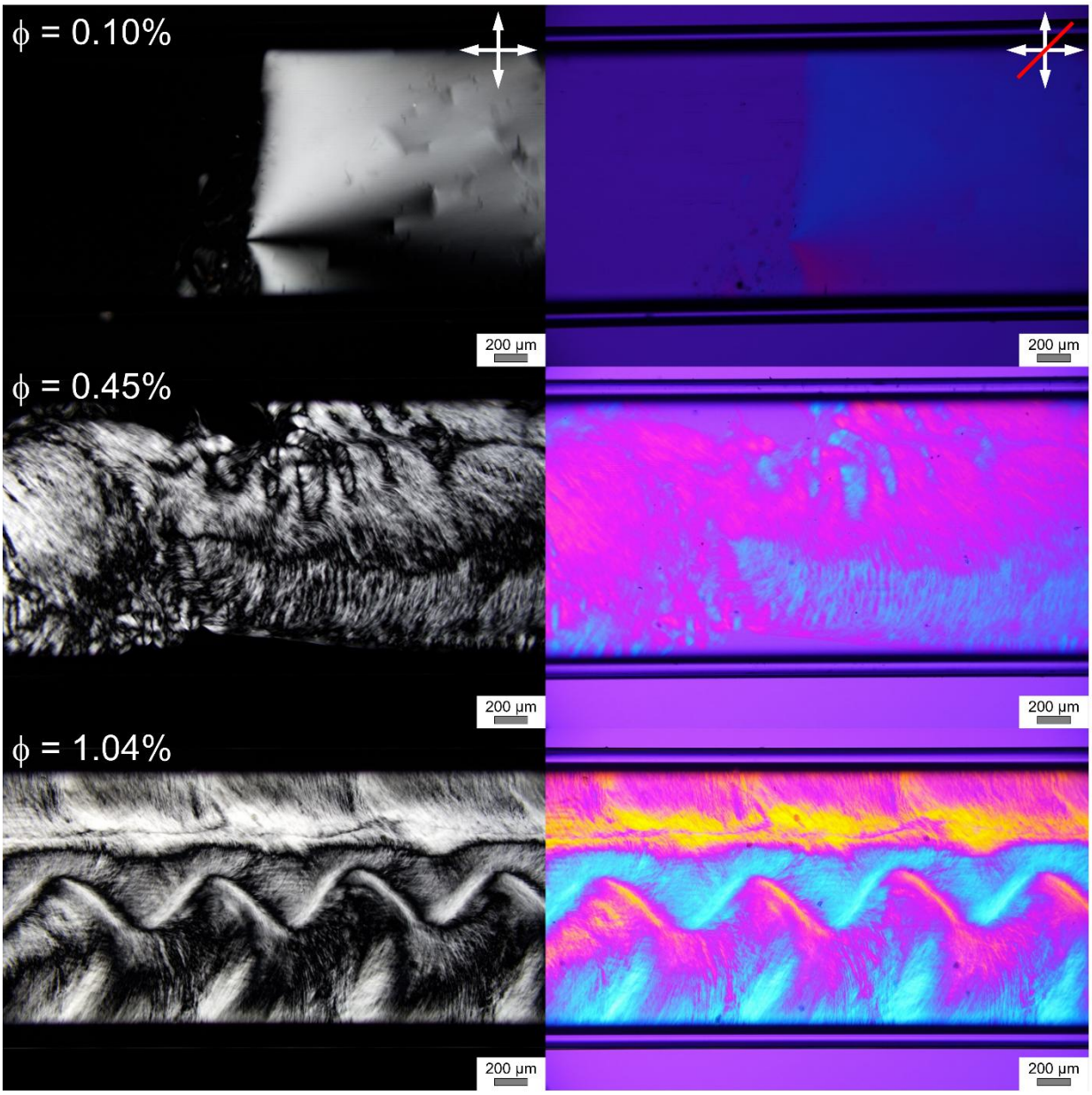

Figure 3. Polarized optical microscopy observations of DW_{20d} aqueous dispersions prepared at different volume fractions ϕ with NaCl (IS = 10^{-3} mol.L^{-1}). The images on the right are taken with the addition of a retardation filter (λ-plate, 530 nm). The white arrows and the red line indicate the orientation of the polarizers and the slow axis of the retardation filter, respectively.

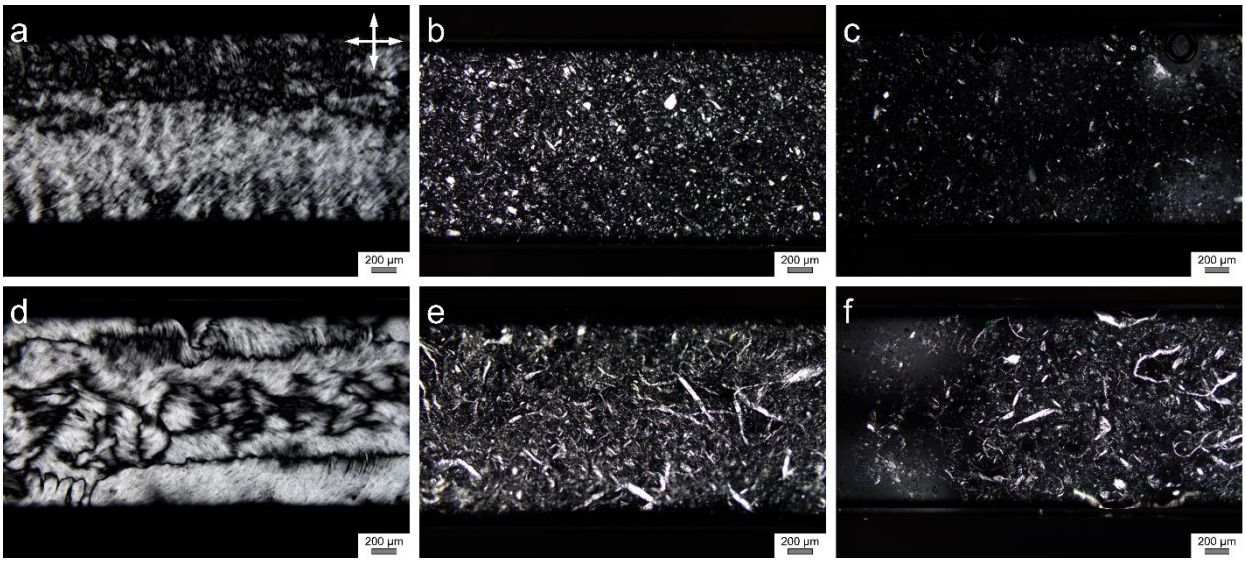

Figure 4. Effect of the electrolyte type on optical textures of (a-c) DW_{5d} (ϕ ~ 0.4%) and (d-f) DW_{20d} (ϕ ~ 0.35%) aqueous dispersions. (a,d) NaCl; (b,e) Na_2SO_4; (c,f) Na_3PO_4.

3.4. Structure of dispersions

Small angle X-ray scattering (SAXS) experiments were conducted to confirm and assess unambiguously the structure of the different dispersions. The measurements were performed after vertical storage of the capillaries for one month to ensure phase separation. When the sample exhibits an isotropic/birefringent phase separation, the scattering intensity shown in the following figures is that of the birefringent part. An example of a scanning along the capillary is presented in Figure S4.

Scattering intensities are first analyzed at a fixed volume fraction, chosen to compare dispersions in multivalent salts with dispersions in NaCl presenting a liquid-crystal organization. As shown in Figure 5, scattering intensities differ significantly between dispersions with monovalent and the multivalent salts. DW dispersions in NaCl present at least four sharp peaks with Q-values following the ratio $1:\sqrt{3}:2:\sqrt{7}$. The ratios between the peak positions correspond to that in a two-dimensional hexagonal reciprocal lattice in the columnar hexagonal (Col_H) phase [34,40,53].

In the middle-Q region [0.01-0.1 $Å^{-1}$], the curve is decreasing as $I(Q) \sim Q^{-1}$, which is typical of one-dimensional objects [54]. By using multivalent salts, the scattering intensity decays as $I(Q) \sim Q^{-2}$, whatever the nanotube aspect ratio. The exponent value of 2 suggests the formation of bi-dimensional aggregates in the system. We also notice the presence of a broad modulation around $Q \sim 6.10^{-3}$ $Å^{-1}$, which could be related to a characteristic average distance in the aggregates.

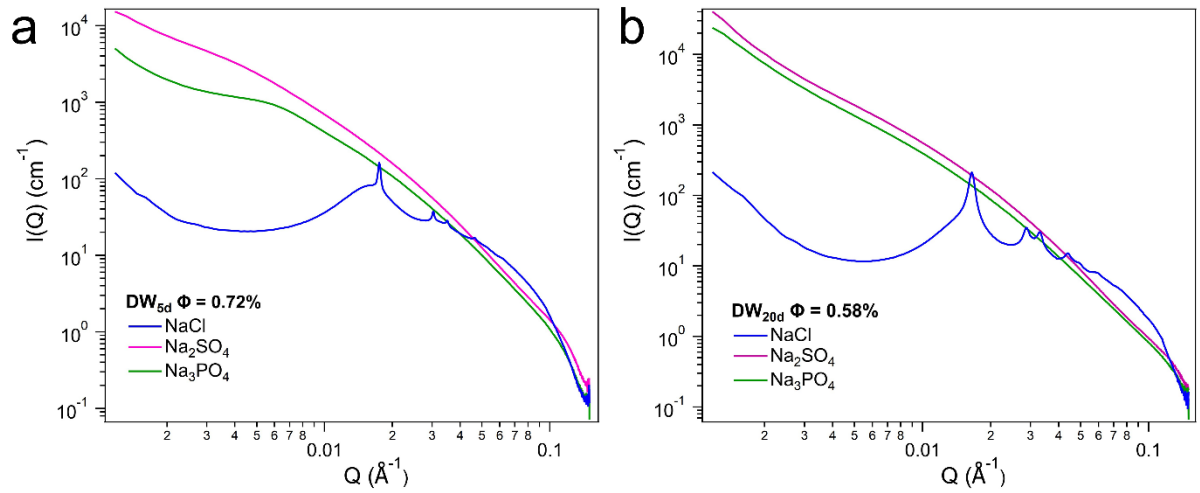

Figure 5. Evolution of the scattering intensity *I(Q)* as a function of the scattering vector *Q* for (a) DW_{5d} and (b) DW_{20d} dispersions prepared in different salts (NaCl, Na_2SO_4 and Na_3PO_4) at a fixed volume fraction of $\phi = 0.72\%$ and $\phi = 0.56\%$ respectively.

In order to magnify the correlation peaks, we have converted the scattered intensities *I(Q)* to obtain the structure factors *Q.I(Q)* for NaCl and $Q^2.I(Q)$ (or Kratky plots) for asymmetric electrolytes (Na_2SO_4 and Na_3PO_4). The resulting curves for the different aspect ratio and volume fractions are presented in Figure 6.

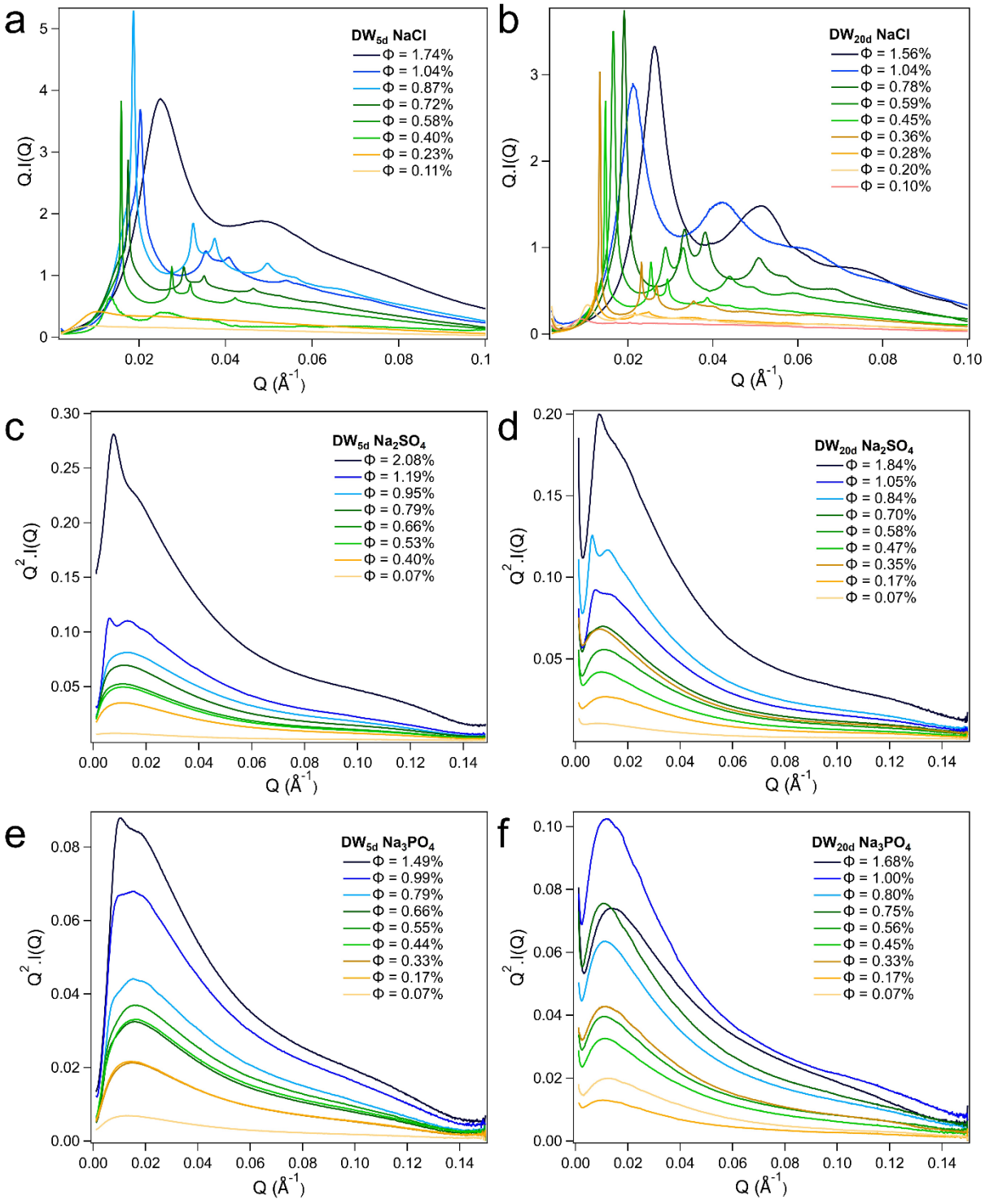

Figure 6. Evolution of the structure factors as a function of the scattering vector *Q* for DW_{5d} (*left*) and DW_{20d} (*right*) dispersions at various volume fractions ϕ with (a,b) NaCl; (c,d) Na_2SO_4 and (e,f) Na_3PO_4 electrolytes.

As anticipated, the evolution of the scattering curves as a function of the volume fraction differ if monovalent anion is used compared to di or trivalent ones, the latter showing only a fairly broad correlation peak. Therefore, bi-dimensional aggregates are present with multivalent salts independently of the volume fraction. For dispersions prepared in NaCl, the SAXS patterns obtained at low volume fractions ($\phi \leq 0.2\%$) present only several broad scattering peaks, arising from short-range positional order of the nanotubes in a nematic phase [11,34]. For higher volume fraction, the observed liquid-crystal phase is of the hexagonal columnar (Col_H) type with the sharp scattering peaks as described above. The positions of these peaks shift towards high Q-region, which corresponds to a decrease of the distance between nanotubes, while increasing concentrations. This is a proof that the interactions are dominated by excluded-volume effects in these dispersions. Finally, once the arrested phase is reached, the scattering curves present only broad periodic modulations of the scattered intensity as in the nematic phase. In this case, the short-range positional order is induced by frustrated orientational and translational motion of the nanotubes in the glass state. Here again, the increase in volume fraction in the arrested phase induces a decrease of the interparticle distance revealed by the shift of the modulations towards high Q-region.

The average interparticle distance $\langle d \rangle$ either in the nematic phase or the arrested phase is calculated from the positions of the first peak as $\langle d \rangle = 2\pi/Q_{max}$. For hexagonal columnar phase, the interparticle distance corresponds to the 2D lattice parameter of the phase $\langle d_{ColH} \rangle$ that can be retrieved by plotting the Q_{hk} vs $\sqrt{h^2 + k^2 + hk}$, with hk the reflections indexed according to a 2D hexagonal lattice. The lattice parameter then depends on the slope γ of this curve as $\langle d_{ColH} \rangle = \frac{4\pi}{\sqrt{3}\gamma}$. For charged nanotubes where the packing entropy term prevails over interparticle

correlations, a 2D hexagonal configuration of parallel nanotubes is expected [55]. This model predicts that the average interparticle distance scales as $\phi^{-0.5}$. Figure 7a shows that experimental interparticle distances obtained at high volume fractions (low $\phi^{-0.5}$ values) display this linear dependence whatever the nanotube aspect ratio.

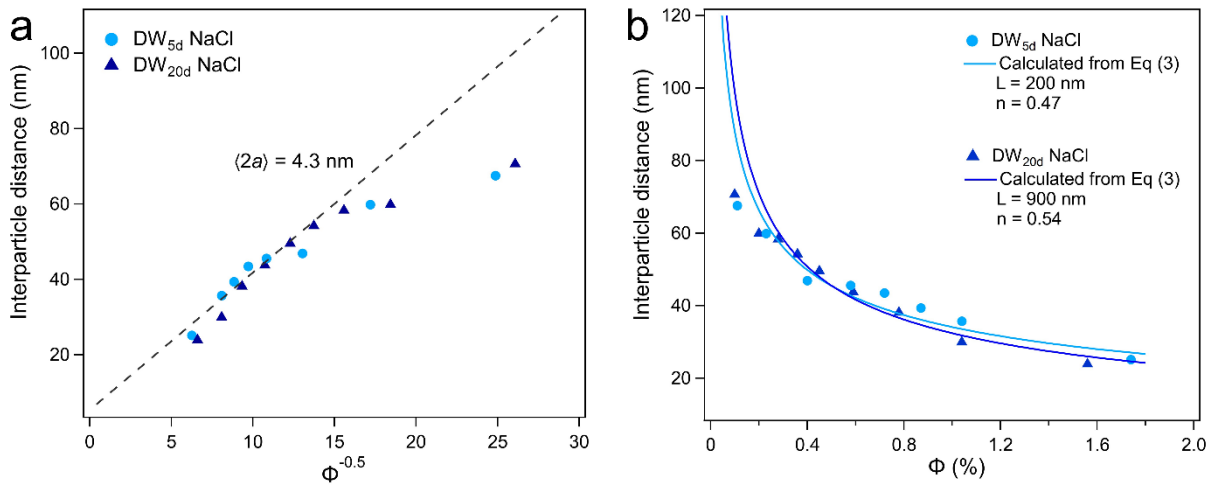

Figure 7. (a) Evolution of the interparticle distance deduced from SAXS curves as a function of $\phi^{-0.5}$. The dotted line corresponds to the model described in Eq. (2). (b) Interparticle distance as a function of Ge-DWINTs volume fraction ϕ. The lines correspond to the fit calculated from Eq. (3).

The deviation for $\phi^{-0.5} \sim 15$ corresponds to the point at which the hexagonal columnar phase predominates, according to POM and SAXS results. We would therefore have a three-dimensional swelling when the nanotubes are in a nematic or isotropic phase. Conversely, the organization of the nanotubes on 2D hexagonal lattice induces a two-dimensional swelling of one-dimensional objects in the direction perpendicular to the nanotube axis. When the glass state is reached, the nanotubes lose degrees of freedom in both rotation and orientation, trapped in a sort of cage defined by their neighbors. In this configuration, the slope of the curve is directly related to the average outer nanotube diameter $\langle 2a \rangle$ [55] such as:

$$\langle d \rangle = \left(\frac{\pi\sqrt{3}}{8}\right)^{\frac{1}{2}} \langle 2a \rangle \phi^{-0.5} \quad (2)$$

By using eq. (2), we find a value of $\langle 2a \rangle$ ~ 4.3 nm, which is in good agreement with the outer diameter of Ge-DWINTs as determined previously [40]. If we perform the same analysis on dispersions prepared with divalent or trivalent electrolytes, the position of the correlation peaks derived from SAXS curves vary widely without any relationship to volume fraction and nanotube aspect ratio (Figure S5). This suggests a heterogeneous aggregation of imogolite nanotubes under current experimental conditions.

A limitation of the model presented in eq. (2) is that it is limited to the high-volume fraction regime and does not reflect the overall trend of the interparticle distances. Baravian *et al.* demonstrated that simple geometrical considerations can predict accurately the evolution of the interparticle distances from the dilute to the concentrated regime [56]. In the case of repulsive 1D objects, the average interparticle distance writes:

$$\langle d \rangle = \frac{L}{\left(\frac{\phi_{eff}}{\phi^*_{eff}}\right)^{1/3} + \left(\frac{\phi_{eff}}{\phi^*_{eff}}\right)^{n}} \quad (3)$$

ϕ_{eff} is the effective volume fraction of a virtual sphere encompassing the particles, which is equivalent to $\phi \frac{2}{3} \left(\frac{L}{\langle 2a \rangle}\right)^2$ for nanotubes where ϕ^*_{eff} is the critical volume fraction corresponding to the packing limit. Baravian *et al.* [56] demonstrated that the maximum packing is ϕ^*_{eff} = 1, considering that the virtual spheres encompassing the particles are deformed leading to a dense packing of prolate ellipsoids [56]. By using this model and the nanotube diameter of 4.3 nm determined previously, the experimental interparticle distances are well reproduced with a value of n ~ 0.5 (i.e. the theoretical value for 1D objects) and an average nanotube length L of 200 and 900 nm for DW_{5d} and DW_{20d}, respectively (Figure 7b). These parameters are similar with the values obtained from TEM analysis and suggests that the fraction of large particles predominates

in the resulting structural organization. Considering the good agreement between experimental and calculated interparticle distances, it is possible to calculate the energy of interactions V between two parallel and charged cylindrical nanoparticles through the DLVO theory [57]. This corresponds to the sum of repulsive electrostatic forces (V_R) due to the diffuse double layer of ions and the van der Waals attractive energy (V_A) that are both dependent of the nanotube length. Details are provided in Supplementary Material. We report in Figure 8 the total energy of interaction per nm (V/L) at T = 298 K and for a ionic strength of $I = 10^{-3}$ mol.L^{-1}. Large repulsive maximum is found at $\langle d \rangle \sim 7.1$-$7.2$ nm. This calculation confirms that for monovalent electrolyte and low ionic strength, imogolites nanotubes are stabilized by strong Coulombic forces via electrical double-layer interactions.

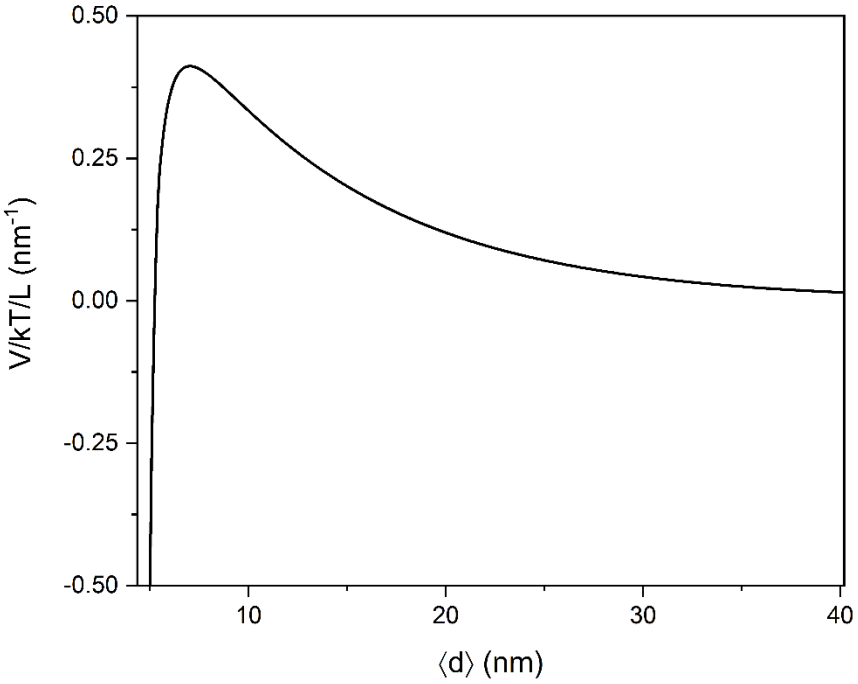

Figure 8. Energy of interaction per nm as a function of the interparticle distance for aqueous dispersions of imogolite nanotubes. Calculations are performed at room temperature for an ionic strength $I = 10^{-3}$ mol.L^{-1}, a surface potential $\psi_0 = 50$ mV, a Hamaker constant $A = 6.7 \times 10^{-20}$ J and a nanotube radius a = 2.2 nm (see text for details).

3.5. Phase diagram

Collectively, these results allow us to build a phase diagram relating the charge valence of salts with respect to the nanotube volume fraction for both aspect ratios (Figure 9). For imogolite nanotubes prepared in asymmetric electrolytes, all our experimental results show a predominance of van der Waals attraction between the nanotubes. Batches with Na_2SO_4 and Na_3PO_4 exhibit similar behavior with the sticking of imogolite nanotubes forming large aggregates that settle down for volume fraction lower than ϕ = 0.2%. Beyond, all the samples form stiff gels, independently of the aspect ratio. The formation of larger aggregates at low ionic strength could be due to a bridging effect between the nanotubes through the di/trivalent ions, also known as the "egg-box" effect [58]. Studies at various ionic strength could be used to determine the critical ionic strength leading to the aggregation of the system and the transition from a glass to a gel state for volume fraction higher than ϕ = 0.2%.

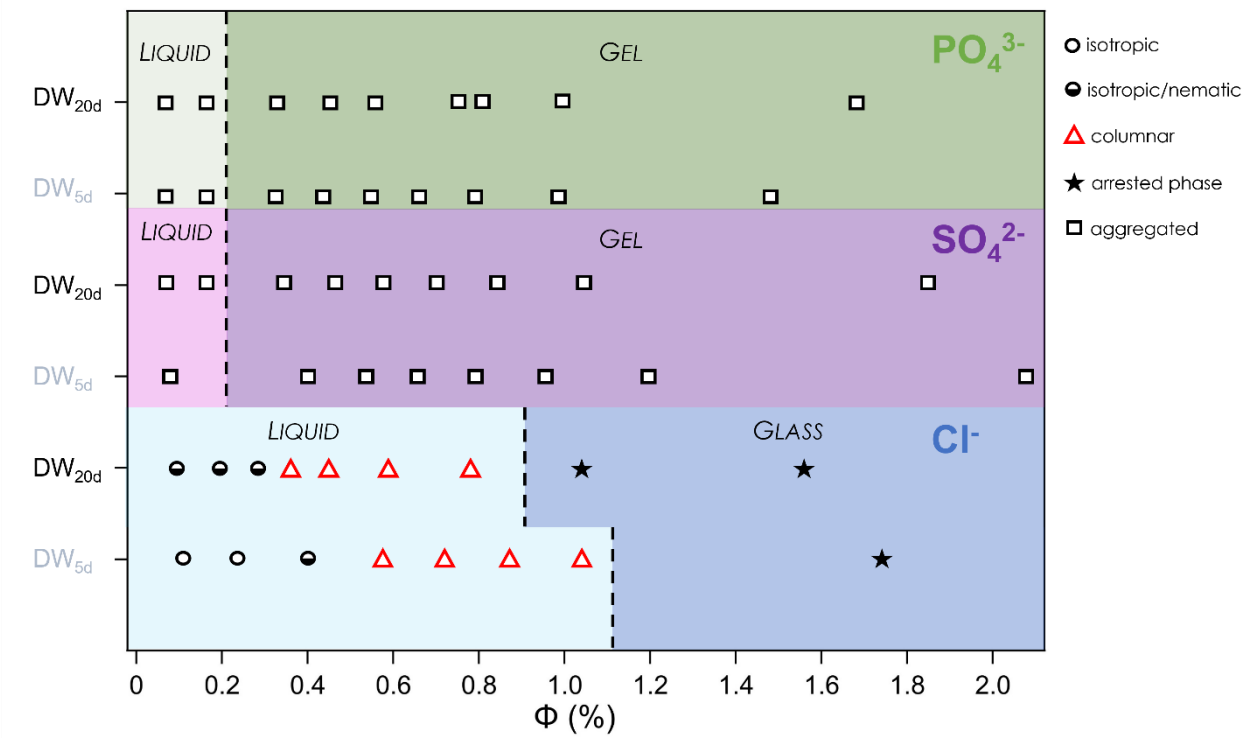

Figure 9. Phase diagram as a function of Ge-DWINTs volume fraction ϕ for DW_{5d} and DW_{20d} with NaCl, Na_2SO_4 and Na_3PO_4 salts. The dotted lines between the different regimes are to guide the eyes.

Imogolite nanotubes dispersed in NaCl present a rich phase diagram with different liquid-crystalline phases (nematic and hexagonal columnar) as a function of the volume fraction. The system becomes totally "frozen" beyond a critical volume fraction, close to 1%. The nanotubes are stiffen into a glass-like state where the tubes are non-aggregated but have limited rotational and translational motion with a nematic-like ordering.

From the phase diagram in Figure 9, we notice that the onsets of the liquid-crystal and sol/glass transitions are shifted to lower volume fraction as the aspect ratio of the nanotubes increases. Typically, the glass-like state is observed at $\phi = 0.9\%$ for DW_{20d} and $\phi = 1.1\%$ for DW_{5d}. This is reminiscent of the theoretical predictions by Vold that the critical volume fraction at which the arrested phase occurs decreases with increasing the particle aspect ratio [59]. Thus, tuning the

nanotube length provides control over the self-organization of imogolite nanotubes and can be used to shift the onset of the arrested phase.

4. Conclusion

We investigated the role of the aspect ratio on the self-organization of anisometric charged nanotubes in presence of symmetric and asymmetric electrolytes at low ionic strength (10^{-3} mol.L^{-1}). We demonstrated that divalent (SO_4^{2-}) or trivalent (PO_4^{3-}) anions induce aggregation of the nanotubes. The formation of aggregates and their related microstructure does not depend on the nanotube aspect ratio nor the volume fraction. This behavior suggests a heterogeneous aggregation process. By contrast, colloidal dispersions of Ge-DWINTs in NaCl display a rich phase behavior with the occurrence of true liquid-crystal phases (nematic and hexagonal columnar phase) before reaching a glassy-like state. We also found that the microstructure is affected by the anisometric nature of the particles, allowing to describe the colloidal organization from the dilute state to the arrested phase. The predominance of repulsive interactions is confirmed from calculations of the interaction potential. The potential decays with decreasing aspect ratio of the nanotubes, increasing the stability range of the liquid-crystal phases before reaching an arrested state. Compared to previous works on colloidal assembly of 1D objects [19,20,24], we have demonstrated that the onset of phase transitions strongly depends on the nanotube aspect ratio; the higher the ratio, the lower the critical volume fraction. This was made possible by the ability to finely control the aspect ratio of the nanotubes during synthesis. This makes imogolite nanotubes attractive as a model system for further experimental and theoretical experiments concerning the colloidal stability of charged 1D nanoparticles and the relation between structure and viscoelastic properties [60,61]. This study open up prospects for probing interactions with more complex electrolytes such as ionic liquids for application in batteries

[62,63]. It also provides new perspectives to develop novel structured materials by triggering the self-organization through external stimuli [64,65].

5. Acknowledgments

The authors acknowledge the SOLEIL synchrotron for allocating beamtime on the SWING beamline (BAG proposal 20221057) and the MORPHEUS platform (LPS, Orsay) for X-ray scattering experiments. This work had benefited from an Investissements d'Avenir grant from Labex PALM (ANR-10-LABX-0039-PALM) and from Imagerie-Gif core facility supported by l'Agence Nationale de la Recherche (ANR-11-EQPX-0029/Morphoscope; ANR-10-INBS-04/FranceBioImaging; ANR-11-IDEX-0003-02/Saclay Plant Sciences).

References

[1] W.J. Stark, P.R. Stoessel, W. Wohlleben, A. Hafner, Industrial applications of nanoparticles, Chem. Soc. Rev. 44 (2015) 5793–5805.
[2] M.J. Mitchell, M.M. Billingsley, R.M. Haley, M.E. Wechsler, N.A. Peppas, R. Langer, Engineering precision nanoparticles for drug delivery, Nat. Rev. Drug Discov. 20 (2021) 101–124.
[3] L. Onsager, The effects of shape on the interaction of colloidal particles, Ann. N. Y. Acad. Sci. 51 (1949) 627–659.
[4] H.H. Wensink, G.J. Vroege, Isotropic-nematic phase behavior of length-polydisperse hard rods, J. Chem. Phys. 119 (2003) 6868–6882. https://doi.org/10.1063/1.1599277.
[5] D. Frenkel, Order through entropy, Nat. Mater. 14 (2015) 9–12.
[6] M.J. Solomon, P.T. Spicer, Microstructural regimes of colloidal rod suspensions, gels, and glasses, Soft Matter 6 (2010) 1391–1400.
[7] N. Miyamoto, T. Nakato, Liquid crystalline inorganic nanosheet colloids derived from layered materials, Isr. J. Chem. 52 (2012) 881–894.
[8] H.N.W. Lekkerkerker, G.J. Vroege, Liquid crystal phase transitions in suspensions of mineral colloids: new life from old roots, Philos. Trans. R. Soc. Math. Phys. Eng. Sci. 371 (2013) 20120263.
[9] I. Dierking, S. Al-Zangana, Lyotropic liquid crystal phases from anisotropic nanomaterials, Nanomaterials 7 (2017) 305.
[10] S.P. Sasikala, J. Lim, I.H. Kim, H.J. Jung, T. Yun, T.H. Han, S.O. Kim, Graphene oxide liquid crystals: a frontier 2D soft material for graphene-based functional materials, Chem. Soc. Rev. 47 (2018) 6013–6045.
[11] P. Davidson, C. Penisson, D. Constantin, J.-C.P. Gabriel, Isotropic, nematic, and lamellar phases in colloidal suspensions of nanosheets, Proc. Natl. Acad. Sci. 115 (2018) 6662–6667.

[12] L.J. Michot, I. Bihannic, S. Maddi, S.S. Funari, C. Baravian, P. Levitz, P. Davidson, Liquid–crystalline aqueous clay suspensions, Proc. Natl. Acad. Sci. 103 (2006) 16101–16104.
[13] L.J. Michot, E. Paineau, I. Bihannic, S. Maddi, J.F.L. Duval, C. Baravian, P. Davidson, P. Levitz, Isotropic/nematic and sol/gel transitions in aqueous suspensions of size selected nontronite NAul, Clay Miner. 48 (2013) 663–685. https://doi.org/10.1180/claymin.2013.048.5.01.
[14] E. Paineau, K. Antonova, C. Baravian, I. Bihannic, P. Davidson, I. Dozov, M. Imperor-Clerc, P. Levitz, A. Madsen, F. Meneau, L.J. Michot, Liquid-Crystalline Nematic Phase in Aqueous Suspensions of a Disk-Shaped Natural Beidellite Clay, J. Phys. Chem. B 113 (2009) 15858–15869.
[15] K. El Rifaii, H.H. Wensink, I. Dozov, T. Bizien, L.J. Michot, J.-C.P. Gabriel, J. Breu, P. Davidson, Do aqueous suspensions of smectite clays form a smectic liquid-crystalline phase?, Langmuir 38 (2022) 14563–14573.
[16] O. Khoruzhenko, D.R. Wagner, S. Mangelsen, M. Dulle, S. Förster, S. Rosenfeldt, V. Dudko, K. Ottermann, G. Papastavrou, W. Bensch, Colloidally stable, magnetoresponsive liquid crystals based on clay nanosheets, J. Mater. Chem. C 9 (2021) 12732–12740.
[17] L.J. Michot, I. Bihannic, K. Porsch, S. Maddi, C. Baravian, J. Mougel, P. Levitz, Phase diagrams of Wyoming Na-montmorillonite clay. Influence of particle anisotropy, Langmuir 20 (2004) 10829–10837.
[18] D. Yamaguchi, N. Miyamoto, T. Fujita, T. Nakato, S. Koizumi, N. Ohta, N. Yagi, T. Hashimoto, Aspect-ratio-dependent phase transitions and concentration fluctuations in aqueous colloidal dispersions of charged platelike particles, Phys. Rev. E 85 (2012) 011403.
[19] Z. Luo, H. Song, X. Feng, M. Run, H. Cui, L. Wu, J. Gao, Z. Wang, Liquid crystalline phase behavior and sol–gel transition in aqueous halloysite nanotube dispersions, Langmuir 29 (2013) 12358–12366.
[20] P. Woolston, J.S. van Duijneveldt, Isotropic-nematic phase transition in aqueous sepiolite suspensions, J. Colloid Interface Sci. 437 (2015) 65–70. https://doi.org/10.1016/j.jcis.2014.09.014.
[21] S. Manzetti, J.-C.P. Gabriel, Methods for dispersing carbon nanotubes for nanotechnology applications: liquid nanocrystals, suspensions, polyelectrolytes, colloids and organization control, Int. Nano Lett. 9 (2019) 31–49.
[22] W. Song, I.A. Kinloch, A.H. Windle, Nematic liquid crystallinity of multiwall carbon nanotubes, Science 302 (2003) 1363–1363.
[23] S. Badaire, C. Zakri, M. Maugey, A. Derré, J.N. Barisci, G. Wallace, P. Poulin, Liquid crystals of DNA-stabilized carbon nanotubes, Adv. Mater. 17 (2005) 1673–1676.
[24] V.A. Davis, A.N.G. Parra-Vasquez, M.J. Green, P.K. Rai, N. Behabtu, V. Prieto, R.D. Booker, J. Schmidt, E. Kesselman, W. Zhou, True solutions of single-walled carbon nanotubes for assembly into macroscopic materials, Nat. Nanotechnol. 4 (2009) 830.
[25] F. Mirri, R. Ashkar, V. Jamali, L. Liberman, R.A. Pinnick, P. Van Der Schoot, Y. Talmon, P.D. Butler, M. Pasquali, Quantification of carbon nanotube liquid crystal morphology via neutron scattering, Macromolecules 51 (2018) 6892–6900.
[26] C.J. Simonsen Ginestra, C. Martínez-Jiménez, A. Matatyaho Ya'akobi, O.S. Dewey, A.D. Smith McWilliams, R.J. Headrick, J.A. Acapulco, L.R. Scammell, M.W. Smith, D.V. Kosynkin,

Liquid crystals of neat boron nitride nanotubes and their assembly into ordered macroscopic materials, Nat. Commun. 13 (2022) 3136.
[27] M.R. Ayatollahi, S. Shadlou, M.M. Shokrieh, M. Chitsazzadeh, Effect of multi-walled carbon nanotube aspect ratio on mechanical and electrical properties of epoxy-based nanocomposites, Polym. Test. 30 (2011) 548–556.
[28] J. Guo, Y. Liu, R. Prada-Silvy, Y. Tan, S. Azad, B. Krause, P. Pötschke, B.P. Grady, Aspect ratio effects of multi-walled carbon nanotubes on electrical, mechanical, and thermal properties of polycarbonate/MWCNT composites, J. Polym. Sci. Part B Polym. Phys. 52 (2014) 73–83.
[29] C. Ding, J. Du, Y. Cao, C. Yue, B. Cheng, Effects of the aspect ratio of multi-walled carbon nanotubes on the structure and properties of regenerated collagen fibers, Int. J. Biol. Macromol. 126 (2019) 595–602.
[30] E. Paineau, G. Monet, V. Peyre, C. Goldmann, S. Rouzière, P. Launois, Colloidal Stability of Imogolite Nanotube Dispersions: A Phase Diagram Study, Langmuir 35 (2019) 12451–12459.
[31] K. Kajiwara, N. Donkai, Y. Hiragi, H. Inagaki, Lyotropic mesophase of imogolite,1. Effect of polydispersity on phase-diagram, Makromol. Chem.-Macromol. Chem. Phys. 187 (1986) 2883–2893.
[32] N. Donkai, K. Kajiwara, M. Schmidt, T. Miyamoto, Lyotropic mesophase of imogolite - molecular-weight fractionation and polydispersity effect, Makromol. Chem.-Rapid Commun. 14 (1993) 611–617.
[33] P. Levitz, M. Zinsmeister, P. Davidson, D. Constantin, O. Poncelet, Intermittent Brownian dynamics over a rigid strand: Heavily tailed relocation statistics in a simple geometry, Phys. Rev. E 78 (2008) 030102. https://doi.org/10.1103/PhysRevE.78.030102.
[34] E. Paineau, M.-E.M. Krapf, M.-S. Amara, N.V. Matskova, I. Dozov, S. Rouzière, A. Thill, P. Launois, P. Davidson, A liquid-crystalline hexagonal columnar phase in highly-dilute suspensions of imogolite nanotubes, Nat. Commun. 7 (2016) 10271. https://doi.org/10.1038/ncomms10271.
[35] C.-Y. Su, Q. Lyu, D.-Y. Kang, Z.-H. Yang, C.H. Lam, Y.-H. Chen, S.-C. Lo, C.-C. Hua, L.-C. Lin, Hexagonal Superalignment of Nano-Objects with Tunable Separation in a Dilute and Spacer-Free Solution, Phys. Rev. Lett. 123 (2019) 238002.
[36] J. Harsh, S. Traina, J. Boyle, Y. Yang, Adsorption of cations on imogolite and their effect on surface-charge characteristics, Clays Clay Miner. 40 (1992) 700–706.
[37] J.P. Gustafsson, The surface chemistry of imogolite, Clays Clay Miner. 49 (2001) 73–80.
[38] N. Arancibia-Miranda, M. Escudey, M. Molina, M. Teresa Garcia-Gonzalez, Use of isoelectric point and pH to evaluate the synthesis of a nanotubular aluminosilicate, J. Non-Cryst. Solids 357 (2011) 1750–1756.
[39] C. Hamon, E. Beaudoin, P. Launois, E. Paineau, Doping liquid crystals of colloidal inorganic nanotubes by additive-free metal nanoparticles, J. Phys. Chem. Lett. 12 (2021) 5052–5058.
[40] E. Paineau, S. Rouzière, G. Monet, C.C. Diogo, I. Morfin, P. Launois, Role of initial precursors on the liquid-crystalline phase behavior of synthetic aluminogermanate imogolite nanotubes, J. Colloid Interface Sci. 580 (2020) 275–285. https://doi.org/10.1016/j.jcis.2020.07.036.

[41] E. Paineau, P. Launois, Influence of the Al/Ge Ratio on the Structure and Self-Organization of Anisometric Imogolite Nanotubes, Crystals 10 (2020) 1094.
[42] T. Cao, M. Elimelech, Colloidal stability of cellulose nanocrystals in aqueous solutions containing monovalent, divalent, and trivalent inorganic salts, J. Colloid Interface Sci. 584 (2021) 456–463.
[43] C. Browne, V.S. Raghuwanshi, G. Garnier, W. Batchelor, Modulating the chiral nematic structure of cellulose nanocrystal suspensions with electrolytes, J. Colloid Interface Sci. 650 (2023) 1064–1072.
[44] W.J. Lee, E. Paineau, D.B. Anthony, Y. Gao, H.S. Leese, S. Rouzière, P. Launois, M.S.P. Shaffer, Inorganic Nanotube Mesophases Enable Strong Self-Healing Fibers, ACS Nano 14 (2020) 5570–5580.
[45] C. Takeshita, K. Masuda, M. Kobayashi, The effect of monovalent anion species on the aggregation and charging of allophane clay nanoparticles, Colloids Surf. Physicochem. Eng. Asp. 577 (2019) 103–109.
[46] M. Li, M. Kobayashi, The aggregation and charging of natural clay allophane: Critical coagulation ionic strength in the presence of multivalent counter-ions, Colloids Surf. Physicochem. Eng. Asp. 626 (2021) 127021.
[47] M. Li, T. Sugimoto, Y. Yamashita, M. Kobayashi, Aggregation and charging of natural allophane particles in the presence of oxyanions, Colloids Surf. Physicochem. Eng. Asp. 649 (2022) 129413.
[48] G. Trefalt, I. Szilagyi, G. Tellez, M. Borkovec, Colloidal stability in asymmetric electrolytes: Modifications of the Schulze–Hardy rule, Langmuir 33 (2017) 1695–1704.
[49] J.F. Moore, E. Paineau, P. Launois, M.S. Shaffer, Continuous Binder-Free Fibers of Pure Imogolite Nanotubes, ACS Appl. Mater. Interfaces 13 (2021) 17940–17947.
[50] M.-S. Amara, E. Paineau, M. Bacia-Verloop, M.-E.M. Krapf, P. Davidson, L. Belloni, C. Levard, J. Rose, P. Launois, A. Thill, Single-step formation of micron long (OH)3Al2O3Ge(OH) imogolite-like nanotubes, Chem. Commun. 49 (2013) 11284–11286.
[51] E. Paineau, M.S. Amara, G. Monet, V. Peyre, S. Rouzière, P. Launois, Effect of Ionic Strength on the Bundling of Metal Oxide Imogolite Nanotubes, J. Phys. Chem. C 121 (2017) 21740–21749.
[52] J. Schindelin, I. Arganda-Carreras, E. Frise, V. Kaynig, M. Longair, T. Pietzsch, S. Preibisch, C. Rueden, S. Saalfeld, B. Schmid, Fiji: an open-source platform for biological-image analysis, Nat. Methods 9 (2012) 676.
[53] F. Camerel, J.-C.P. Gabriel, P. Batail, P. Davidson, B. Lemaire, M. Schmutz, T. Gulik-Krzywicki, C. Bourgaux, Original Single Walled Nanotubules Based on Weakly Interacting Covalent Mineral Polymers, 1∞[Nb2PS10-] in N-Methylformamide, Nano Lett. 2 (2002) 403–407.
[54] A. Guinier, G. Fournet, K.L. Yudowitch, Small-angle scattering of X-rays, (1955).
[55] E.E. Maier, R. Krause, M. Deggelmann, M. Hagenbuechle, R. Weber, S. Fraden, Liquidlike order of charged rodlike particle solutions, Macromolecules 25 (1992) 1125–1133.
[56] C. Baravian, L.J. Michot, E. Paineau, I. Bihannic, P. Davidson, M. Imperor-Clerc, E. Belamie, P. Levitz, An effective geometrical approach to the structure of colloidal suspensions of very anisometric particles, Epl 90 (2010) 36005. https://doi.org/10.1209/0295-5075/90/36005.

[57] P.A. Buining, A.P. Philipse, H.N.W. Lekkerkerker, Phase behavior of aqueous dispersions of colloidal boehmite rods, Langmuir 10 (1994) 2106–2114.
[58] G. Lagaly, I. Dékány, Colloid clay science, in: Dev. Clay Sci., Elsevier, 2013: pp. 243–345.
[59] M.J. Vold, Sediment volume and structure in dispersions of anisometric particles, J. Phys. Chem. 63 (1959) 1608–1612.
[60] T. Narayanan, H. Wacklin, O. Konovalov, R. Lund, Recent applications of synchrotron radiation and neutrons in the study of soft matter, Crystallogr. Rev. 23 (2017) 160–226.
[61] M. Gvaramia, G. Mangiapia, V. Pipich, M.-S. Appavou, S. Jaksch, O. Holderer, M.D. Rukhadze, H. Frielinghaus, Tunable viscosity modification with diluted particles: when particles decrease the viscosity of complex fluids, Colloid Polym. Sci. 297 (2019) 1507–1517.
[62] A.K. Tripathi, Ionic liquid–based solid electrolytes (ionogels) for application in rechargeable lithium battery, Mater. Today Energy 20 (2021) 100643.
[63] N. Kapernaum, A. Lange, M. Ebert, M.A. Grunwald, C. Haege, S. Marino, A. Zens, A. Taubert, F. Giesselmann, S. Laschat, Current topics in ionic liquid crystals, ChemPlusChem 87 (2022) e202100397.
[64] Y. Zhao, G. Cavallaro, Y. Lvov, Orientation of charged clay nanotubes in evaporating droplet meniscus, J. Colloid Interface Sci. 440 (2015) 68–77.
[65] C. Bruel, T.S. Davies, P.J. Carreau, J.R. Tavares, M.-C. Heuzey, Self-assembly behaviors of colloidal cellulose nanocrystals: A tale of stabilization mechanisms, J. Colloid Interface Sci. 574 (2020) 399–409.

Figure captions

Figure 1. Representative TEM images of Ge-DWINTs batches obtained after (a) 5 days and (b) 20 days of hydrothermal reaction. Corresponding histograms of length distribution for (c) DW_{5d} and (d) DW_{20d}.

Figure 2. Macroscopic optical observations between crossed polarizers of (a-c) DW_{5d} and (d-f) DW_{20d} aqueous dispersions prepared at different volume fractions ϕ and electrolytes (IS = 10^{-3} $mol.L^{-1}$). (a,d) NaCl; (b,e) Na_2SO_4; (c,f) Na_3PO_4. Photographs of DW_{20d} aqueous dispersions with NaCl (g) in a liquid state (ϕ = 0.36%) and (h) above the glass transition (ϕ = 0.94%). The latter does not flow upon tube reversal.

Figure 3. Polarized optical microscopy observations of DW_{20d} aqueous dispersions prepared at different volume fractions ϕ with NaCl (IS = 10^{-3} $mol.L^{-1}$). The images on the right are taken with the addition of a retardation filter (λ-plate, 530 nm). The white arrows and the red line indicate the orientation of the polarizers and the slow axis of the retardation filter, respectively.

Figure 4. Effect of the electrolyte type on optical textures of (a-c) DW_{5d} ($\phi \sim 0.4\%$) and (d-f) DW_{20d} ($\phi \sim 0.35\%$) aqueous dispersions. (a,d) NaCl; (b,e) Na_2SO_4; (c,f) Na_3PO_4.

Figure 5. Evolution of the scattering intensity *I(Q)* as a function of the scattering vector *Q* for (a) DW_{5d} and (b) DW_{20d} dispersions prepared in different salts (NaCl, Na_2SO_4 and Na_3PO_4) at a fixed volume fraction of ϕ = 0.72% and ϕ = 0.56% respectively.

Figure 6. Evolution of the structure factors as a function of the scattering vector Q for DW_{5d} (*left*) and DW_{20d} (*right*) dispersions at various volume fractions ϕ with (a,b) NaCl; (c,d) Na_2SO_4 and (e,f) Na_3PO_4 electrolytes.

Figure 7. (a) Evolution of the interparticle distance deduced from SAXS curves as a function of $\phi^{-0.5}$. The dotted line corresponds to the model described in Eq. (2). (b) Interparticle distance as a function of Ge-DWINTs volume fraction ϕ. The lines correspond to the fit calculated from Eq. (3).

Figure 8. Energy of interaction per nm as a function of the interparticle distance for aqueous dispersions of imogolite nanotubes. Calculations are performed at room temperature for an ionic strength $I = 10^{-3}$ mol.L^{-1}, a surface potential $\psi_0 = 50$ mV, a Hamaker constant $A = 6.7 \times 10^{-20}$ J and a nanotube radius a = 2.2 nm (see text for details).

Figure 9. Phase diagram as a function of Ge-DWINTs volume fraction ϕ for DW_{5d} and DW_{20d} with NaCl, Na_2SO_4 and Na_3PO_4 salts. The dotted lines between the different regimes are to guide the eyes.

Supplementary material

Colloidal phase behavior of high aspect ratio clay nanotubes in symmetric and asymmetric electrolytes

Claire HOTTON[a,*], Léna LE ROUX[a], Claire GOLDMANN[a], Stéphan ROUZIÈRE[a], Pascale LAUNOIS[a], Thomas BIZIEN[b], Erwan PAINEAU[a,*]

1. Characterization of Ge-DWINTs batches

Fourier Transform Infrared (FTIR) spectroscopy was realized on KBr pressed pellets containing ~ 1%wt of Ge-DWINTs powder. Acquisitions were performed with a Nicolet iS50 FTIR spectrometer equipped with a KBr beamsplitter and a DTGS/KBr detector. The resulting FTIR spectra correspond to the average of 64 scans at a resolution of 4 cm^{-1}. The obtained spectra (Figure S1a) display the vibrations of imogolite nanotubes at 910 cm^{-1} and the characteristic doublet at 830/805 cm^{-1} related to the local structure of aluminogermanate imogolite nanotubes. These vibrations are assigned to Ge-O stretching in isolated GeO_4 structures, while the absorption bands at 690, 555 and 420 cm^{-1} are related to Al-O vibrations in the INT structure.[S1,S2] In addition, FTIR curves present two broad peaks at 3580 and 3400 cm^{-1} that are related to O-H stretching (OHν) of outer and inner hydroxyl groups.

Characterization of synthetic Ge-DWINTs was completed by laboratory X-ray scattering (XRS) on the MORPHEUS platform at Laboratoire de Physique des Solides. Experiments were realized on a rotating anode generator (RU H3R, Rigaku Corp., Japan) operating at the Cu$K\alpha$ wavelength delivered by Osmic optics. Powder samples were packed in borosilicate glass capillaries (WJMGlas/Müller GmbH, Germany) and placed at a sample-to-detector distance of 250 mm. The scattering signals were collected on a two-dimensional mar345 image plate detector (marXperts GmbH, Germany) with a 150 µm pixel size. Angular integration of the 2D patterns were performed to obtain the dependence of the scattered intensity I(Q) presented in Figure S1b. The diffractograms show large oscillations related to the form factor of a tubular structure as detailed previously.[S3] In particular, the enhanced intensity between 0.4 and 0.9 $Å^{-1}$ is characteristic of the mean inter-wall distance in a double-walled nanotube.[S4,S5] The 002 asymmetric peak around 1.5 $Å^{-1}$ is a signature of the one-dimensional periodicity along the nanotube axis,[S6] the period being equal to ~ 8.5 Å.

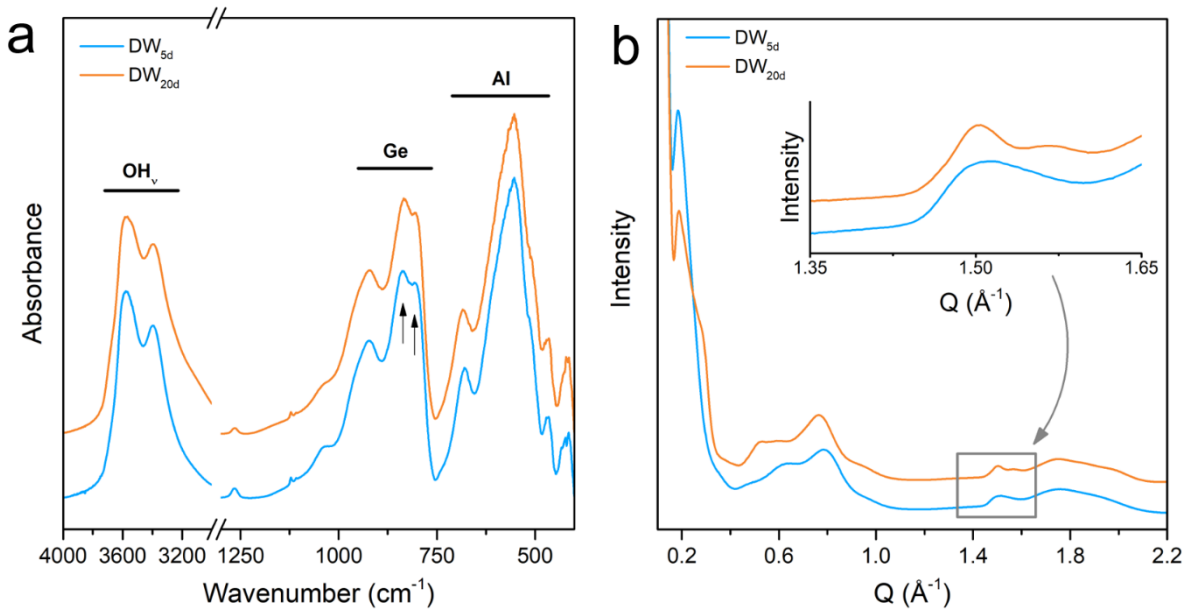

Fig. S1. (a) FTIR spectra and (b) X-ray scattering patterns of Ge-DWINTs feedstocks. The curves are translated for the sake of clarity. The two black arrows in panel (a) highlight the characteristic doublet at 830/805 cm^{-1} related to the local structure of aluminogermanate imogolite nanotubes. The inset in panel (b) is an enlarge view around the 002 asymmetric peak characteristic of the nanotube periodicity.

2. Polarized optical microscopy

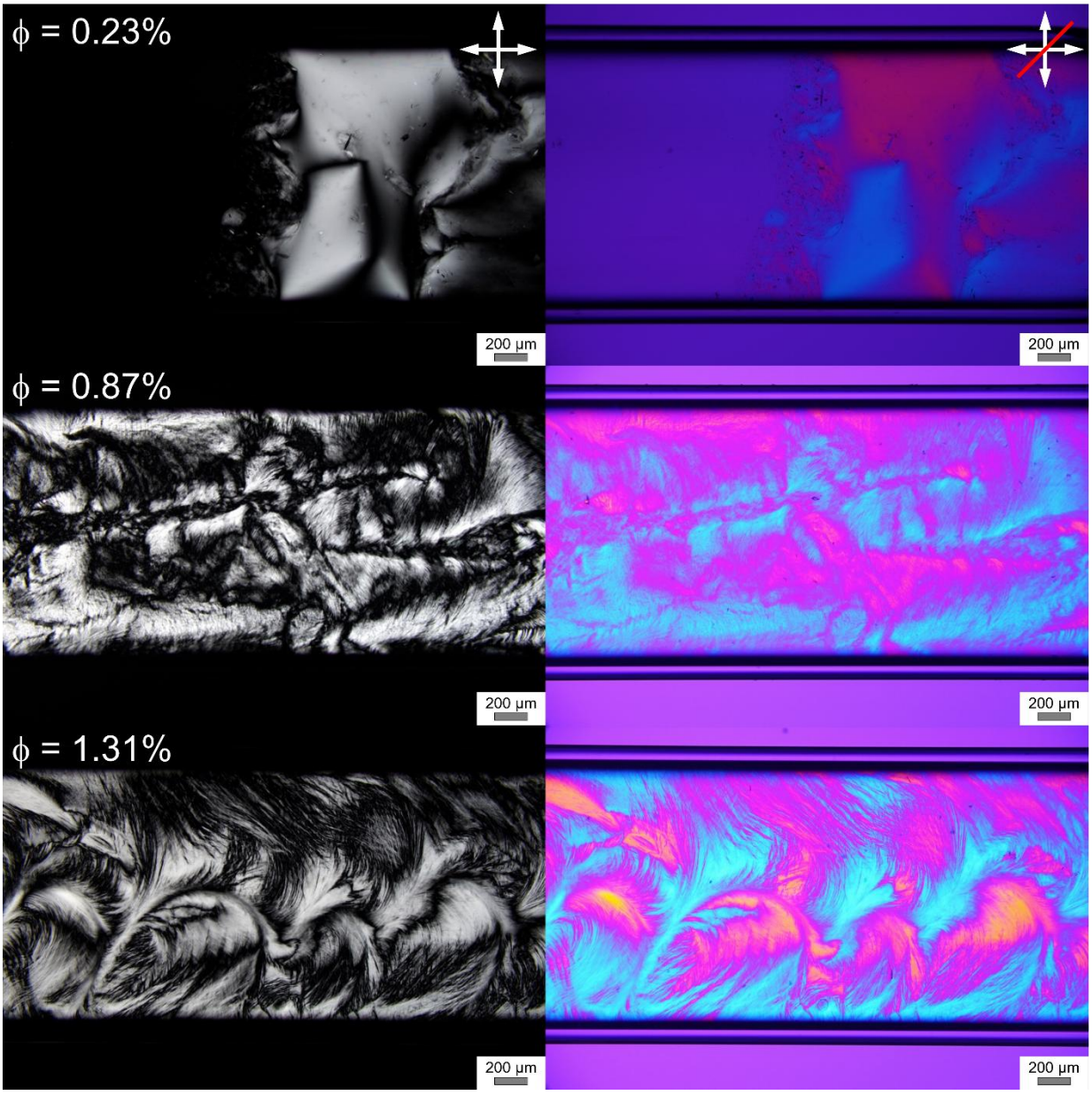

Fig. S2. Polarized optical microscopy observations of DW_{5d} aqueous dispersions prepared at different volume fractions ϕ with NaCl (IS = 10^{-3} mol.L^{-1}). The images are taken (*left*) without and (*right*) with the addition of a retardation filter (λ-plate, 530 nm). The white arrows and the red line indicate the orientation of the polarizers and the slow axis of the retardation filter, respectively.

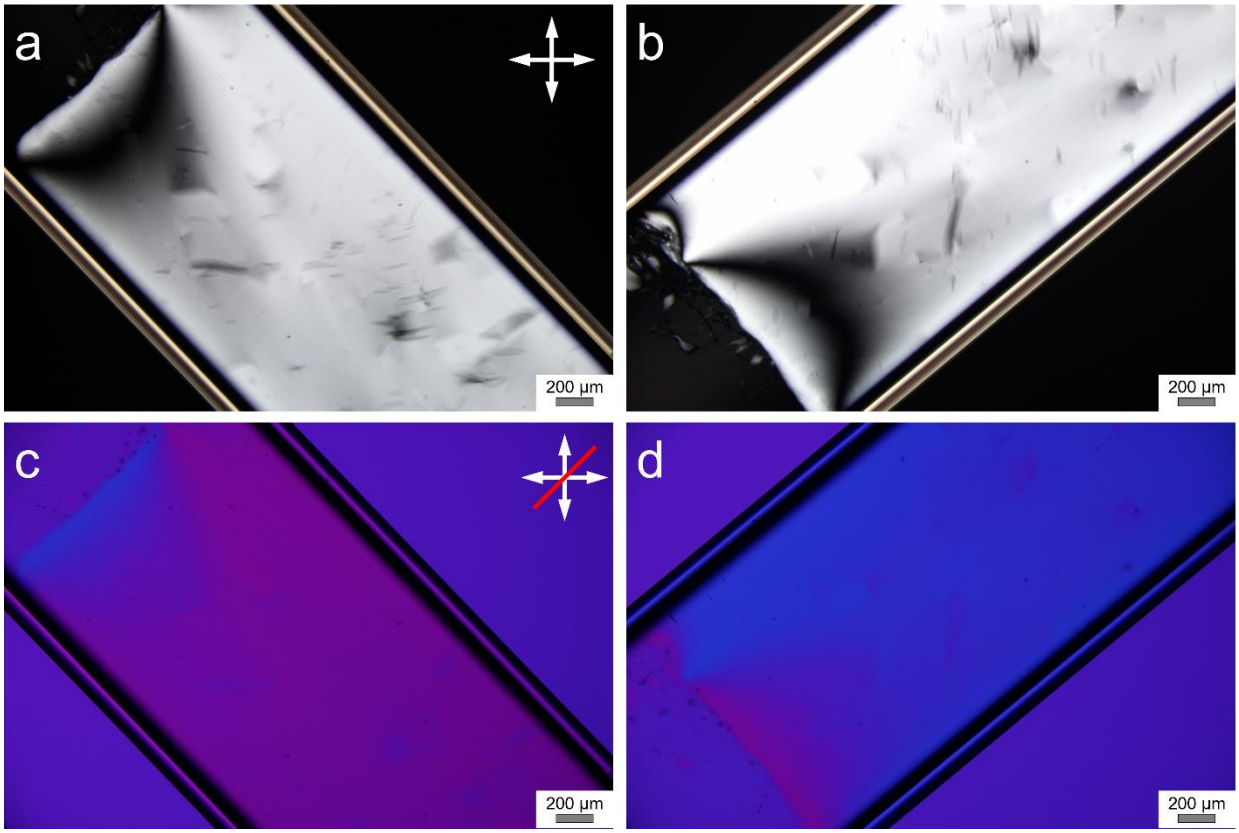

Fig. S3. Optical textures in polarized light microscopy of DW_{20d} aqueous dispersions (ϕ = 0.1%, [NaCl] = 10^{-3} mol.L^{-1}) without (a,b) and with (c,d) a retardation filter (λ-plate, 530 nm). The sample is tilted by 45° clockwise (a,c) and counter-clockwise (b,d). The white arrows and the red line indicate the orientation of the polarizers and the slow axis of the retardation filter, respectively.

3. Scanning along the capillary by Small Angle X-ray Scattering

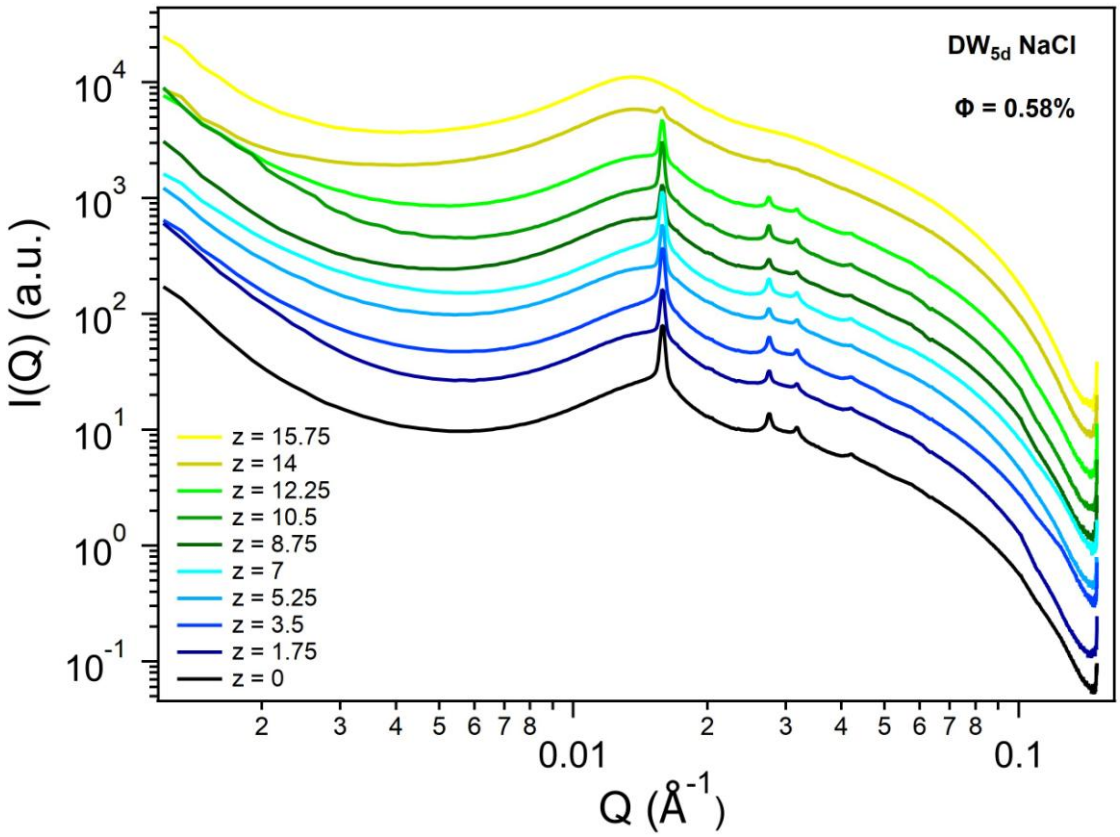

Fig. S4. Evolution of the scattering intensity I(Q) as a function of the scattering vector Q along the capillary (from top at z = 15.75 mm corresponding to the yellow curve to bottom at z = 0 mm corresponding to the black curve) of a DW_{5d} dispersion prepared in NaCl at a volume fraction of 0.58%. All curves have been shifted vertically for the sake of clarity.

4. Swelling laws

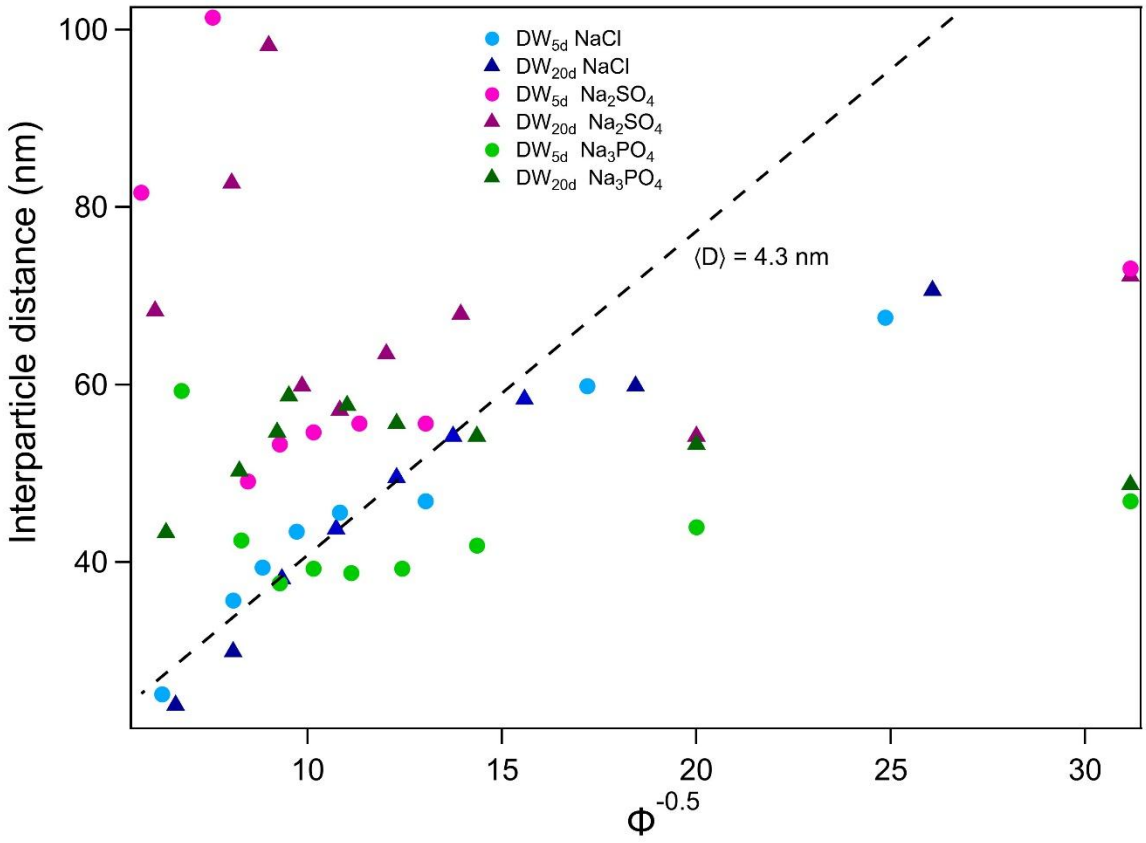

Fig. S5. Evolution of the interparticle distance with $\phi^{-0.5}$ for aqueous dispersions of DW_{5d} (circles) and DW_{20d} (triangles) as a function of the electrolytes (IS = 10^{-3} mol.L^{-1}). The dashed line corresponds to the packing of the nanotubes assuming a 2D hexagonal configuration and a nanotube diameter of 4.3 nm.

5. DLVO calculations

For a symmetric electrolyte such as NaCl, it is possible to calculate the energy of interactions between two charged cylindrical nanoparticles through the DLVO theory. This corresponds to the sum of repulsive electrostatic forces (V_R) due to the diffuse double layer of ions and the van der Waals attractive energy (V_A). Since the nanotubes present preferential orientation, we can assume in a first approximation that they lie parallel. In this case, the repulsive energy for charged cylinders of aspect ratio $L/2a$ is given by the expression[S7]:

$$V_R = 64\pi^{1/2} nkT \left(\tanh\left(\frac{e\psi_0}{4kT}\right)\right)^2 L \frac{(\kappa a)^{1/2}}{\kappa^2} e^{-\kappa(\langle d\rangle - \langle 2a\rangle)} \qquad (SI1)$$

with n the number density of ions in the suspension, e the proton charge and ψ_0 the particle surface potential. We take ψ_0 = 50 mV deduced from previous zeta-potential measurements on DWINTs.[S2] κ is the inverse of the Debye screening length of the diffuse double layer, which for 1:1 electrolytes is $\sqrt{I}/0.304 \times 10^{-9}$ (nm^{-1}). For the van der Waals attractive energy, the expression depends on the interparticle distance $\langle d\rangle$. For short values (typically $(\langle d\rangle - \langle 2a\rangle) \ll a$), the attractive term is:

$$V_A = -\frac{A}{24}\frac{L}{a}\left(\frac{a}{\langle d\rangle - \langle 2a\rangle}\right)^{\frac{3}{2}}\left(1 - \frac{9}{8}\frac{\langle d\rangle - \langle 2a\rangle}{a}\right) \qquad (SI2)$$

with A the Hamaker constant. For larger interparticle distances, the expression of V_A becomes:

$$V_A = -\frac{3\pi}{8} A \frac{L}{a} a^5 U_5 \qquad (SI3)$$

where U_5 is a function which depends on the cylinder radius and the distance $\langle d\rangle$ between the cylinder axes and which can be developed in a series of $\frac{a}{\langle d\rangle}$ as detailed in ref. [S7]. The Hamaker constant of imogolite nanotubes being never estimated, we have used the value reported for AlO(OH) nanorods ($A = 6.7 \times 10^{-20}$ J),[s8] assuming the aluminum outer surface of imogolite nanotubes to be close to boehmite. Similar values of V_A are obtained from eq. (SI2) and (SI3) for $\langle d\rangle - \langle 2a\rangle = a/2$, which is the crossover value chosen for using one or the other equation to calculate the total energy of interaction $V = V_R + V_A$.

6. Additional references

[S1] S. Wada, K. Wada, Effects of substitution of germanium for silicon in imogolite, Clays Clay Miner. 30 (1982) 123–128.

[S2] E. Paineau, S. Rouzière, G. Monet, C.C. Diogo, I. Morfin, P. Launois, Role of initial precursors on the liquid-crystalline phase behavior of synthetic aluminogermanate imogolite nanotubes, J. Colloid Interface Sci. 580 (2020) 275–285.

[S3] E. Paineau, G. Monet, V. Peyre, C. Goldmann, S. Rouzière, P. Launois, Colloidal Stability of Imogolite Nanotube Dispersions: A Phase Diagram Study, Langmuir 35 (2019) 12451–12459.

[S4] J. Cambedouzou, M. Chorro, R. Almairac, L. Noé, E. Flahaut, S. Rols, M. Monthioux, P. Launois, X-ray diffraction as a tool for the determination of the structure of double-walled carbon nanotube batches, Phys. Rev. B 79 (2009) 195423.

[S5] P. Maillet, C. Levard, E. Larquet, C. Mariet, O. Spalla, N. Menguy, A. Masion, E. Doelsch, J. Rose, A. Thill, Evidence of Double-Walled Al-Ge Imogolite-Like Nanotubes. A Cryo-TEM and SAXS Investigation, J. Am. Chem. Soc. 132 (2010) 1208–1209.

[S6] G. Monet, M.S. Amara, S. Rouzière, E. Paineau, Z. Chai, J.D. Elliott, E. Poli, L.-M. Liu, G. Teobaldi, P. Launois, Structural resolution of inorganic nanotubes with complex stoichiometry, Nat. Commun. 9 (2018) 2033.

[S7] P.A. Buining, A.P. Philipse, H.N.W. Lekkerkerker, Phase behavior of aqueous dispersions of colloidal boehmite rods, Langmuir 10 (1994) 2106–2114.

[S8] R.G. Horn, D.R. Clarke, M.T. Clarkson, Direct measurement of surface forces between sapphire crystals in aqueous solutions, J. Mater. Res. 3 (1988) 413–416.